Additive Manufacturing 57 (2022) 102934

Contents lists available at ScienceDirect

Additive Manufacturing

journal homepage: www.elsevier.com/locate/addma

Kinetic evaluation of the starch molecular behavior under extrusion-based or laser powder bed fusion 3D printing systems: A systematic structural and biological comparison

Mahdiyar Shahbazi [a,*,1], Henry Jäger [a,**], Rammile Ettelaie [b]

[a] Institute of Food Technology, University of Natural Resources and Life Sciences (BOKU), Muthgasse 18, 1190 Vienna, Austria
[b] Food Colloids Group, School of Food Science and Nutrition, University of Leeds, Leeds LS2 9JT, UK

ARTICLE INFO

Keywords:
3D printing
Crosslinking
Size exclusion chromatography
Crystallinity
Frequency sweep

ABSTRACT

Supramolecular polymers are the most used materials for 3D printing applications because of their ability to improve the flow behavior of inks, and consequently enhance the mechanical strength of printed architectures. However, their interactions are assessed without considering the fact that their formed structures are affected by the printing process. Here, the effects of printer temperature of an extrusion-based printing system, or surface temperature of a laser powder bed fusion printer, on the molecular behavior of starch were investigated. Starch, being a highly branched polymer, was selected as the tested biopolymer since it provides numerous noteworthy benefits for an investigation of the depolymerization/crosslinking mechanisms upon printing, which could shed light on the impact of 3D printing on non-degradable materials. Completely different behaviors of starch functional properties are found between the two printing systems, where the extrusion-based printer promoted a significant degradation of the starch chains, while the laser powder bed fusion offered a typical behavior associated with crosslinking/branching. Extrusion 3D printing induced a reduction in starch molecular size and therefore in the structural strength of networks formed from it. However, this was also found to increase the starch digestibility rate/extent. In contrast, laser powder bed fusion increased the molecular size, inducing a viscoelastic gel-like character. At the same time, it decreased the starch digestion rate/extent. The obtained data offers information that can support the mechanistic interpretation of the depolymerization/crosslinking kinetics on the non-degradable materials, where it may be much harder to obtain the branch-length distribution. Therefore, the mechanistic information provided from starch can also be useful in understanding the degradation/chain branching of synthetic branched polymers undergoing the same printing processes.

1. Introduction

Three-dimensional (3D) printing has revolutionized prototyping and has found applications in many fields of industry because of the decreasing fabrication prices of the 3D printing systems, enhanced printing resolution, and fast process speeds [1–3]. Nowadays, numerous 3D printing systems exist in the marketplace to develop functional 3D printed structures. Each 3D printing process offers its own distinct advantages and limitations, which affect the 3D printing of the end product. A review of the desirable and less wanted features for different types of systems was published elsewhere [2,4]. The extrusion-based 3D printing is the most extensively employed system in additive manufacturing, giving the rapid prototyping and processability of various materials at a low cost [2,5,6]. During extrusion 3D printing, the polymers are subjected to large amounts of shearing force, high temperatures, and pressure conditions. All of these can change the functional properties of the polymers. The degree to which the molecular chains are degraded during the extrusion printing can be considered to be an important parameter in determining the suitability of such polymeric molecules in the construction of 3D structures. Laser powder bed fusion (LPBF), being the third most common 3D printing method [6], constitutes a subdivision of powder bed fusion additive manufacturing.

---

* Corresponding author.
** Corresponding author at: Institute of Food Technology, Department of Food Science and Technology, University of Natural Resources and Life Sciences, Muthgasse 18, 1190 Vienna, Austria.
E-mail addresses: mahdiyar.shahbazi@boku.ac.at, shahbazim00@yahoo.com (M. Shahbazi), henry.jaeger@boku.ac.a (H. Jäger).
[1] https://orcid.org/0000-0002-2485-9130

https://doi.org/10.1016/j.addma.2022.102934
Received 1 January 2022; Received in revised form 16 May 2022; Accepted 25 May 2022

It uses a laser beam (like a CO_2 laser) as the heating source to fuse and sinter granular powder thermoplastic compounds in a layer-by-layer fashion [7–9]. The LPBF printing system is equipped with an infrared radiation light source to preheat the powder bed. The top layer of the powder is heated up to a temperature slightly below the melting temperature of the sintered materials. The sintering process includes a repetitive powder deposition, in which the preheated particles are selectively melted by a CO_2 laser between each powder application. It is well-known that many factors, including the type of printer, printing process parameters, and the materials itself can influence the 3D printing process and hence the quality of the 3D printed parts [1,5,7]. Accordingly, appropriate systematic approaches become essential to specify how desirable possible alterations in the functional features of the polymers can be brought about.

Even though biomaterials are affected by 3D printing techniques, where their functional properties are changed, the molecular alteration of biomaterials upon different conditions of the 3D printing process has not been adequately addressed. Regarding extrusion-based dispensing module, degradation of the molecular chains upon melt extrusion is a recognized matter [1,6,8]. Therefore, once biomaterials are utilized in an extrusion-based printer, the evaluation of their degradability is imperative as any depolymerization can lead to undesirable issues during the printing process. Reportedly, a great reduction in viscoelasticity, and the molecular weight of the biodegradable polymers, have been observed in this type of printing system [1–3,5]. In the case of LPBF, the biopolymers are exposed to substantial thermally induced stresses [9,10]. During LPBF printing, a polymer can be subjected to physical melting or physical or chemical crosslinking depending on the nature of polymers and processing parameters [9,11]. The sintering process melts the solid polymer to a liquid phase under the application of a CO_2 laser; next, the inter- and intramolecular crosslinking can be developed between polymeric strands, becoming rearranged in an ordered pattern. This changes the degree and extent of the crystallization and the crystal integrity [7,9,11].

Starch has the advantage that the distribution of the degree of polymerization of individual branches can be simply obtained. More importantly, it also does not undergo any complex chemical reactions, except for simple chain scission (or crosslinking) during the printing process. This greatly aids the mechanistic interpretation of the results for this biopolymer, undergoing a 3D printing process. In starch, the nonoverlapping spatial chain distributions of amylose (long-chain branching) and amylopectin (short-chain branching) offer an insight into the impacts of the overall sizes and chain lengths to be ascertained [12]. Polyolefins, by contrast, have no important alteration in size distributions of differently branched chains. Furthermore, there is a substantial reaction effect of the unsaturated end-groups during the 3D printing of polyolefins [8–11]. In contrast, starch, at the end of each branch, contains fundamentally “nonreducing” ends (glucose units with an α-(1,4) glycosidic bond to the preceding glucose residue), and per the whole molecule, has a single “reducing” end-group (a 6-membered ring with three adjacent hydroxyl groups that could ring-open to a free aldehyde-keto group). In starch, the mentioned end-groups cannot undergo reaction during 3D printing. Thermo-oxidative reactions, crosslinking, and side-chain branching happen along with simple scission in the extrusive/thermal depolymerization of polyolefins. This may lead to an increase in molecular weight and size where the overall size distribution, emerging from the printing process, can be the result of a competition between this increase and the simultaneously occurring decrease due to the simple shear scission [12]. Concerning starch, only simple scission and degradation occur, therefore allowing a more straightforward interpretation of results arising from a reduction in the molecular weight and the size only. In other words, a molecular investigation of starch during extrusion printing allows the mechanisms, which only involve simple scission to be elaborated in isolation.

The LPBF technology offers the possibility to remove the thermal depolymerization of sintered biomaterials through localizing the heating process on their surfaces only. This can be accomplished through the selective absorption of mid-infrared laser radiation [13] with a thin layer of water droplets placed on the surfaces of biopolymeric particles, or the usage of a hygroscopic coating that absorbs the energy of laser irradiation better than the biopolymeric compound itself. It is always difficult to predict the existence of crosslinking or degradation reactions upon sintering. This depends on many factors such as the type of printable materials, moisture content, existence of the additive compounds, temperature, and the processing time. There are several reports in the literature, that state a crosslinking reaction increases the molecular weight of some polymers [9–11,14]. In contrast, a decrease in the molecular weight via sintering was found after processing, thus confirming chain scission induced by thermal stresses [15,16].

To obtain sufficient knowledge about the 3D printing process so as to improve the printing quality, a mechanistic approach to understanding the effect of process conditions during extrusion and LPBF on the molecular behavior of starch is needed. Additional investigation regarding the molecular behavior of starch upon processing can be established by examining the starch viscoelastic behavior, crystalline pattern, proton mobility, thermal behavior, and biological features. It has been revealed that change in the molecular structure during processing correlates well with the rheological, crystalline, and biological properties (like digestion feature) of starch [17,18].

In view of the limitation in the existing research concerning the impact of the changes in the molecular size/weight of biopolymers, occurring during the 3D printing process, the present work aimed to investigate the influence of printing temperature of an extrusion-based 3D printing system or the surface temperature of an LPBF 3D printer on the functional properties of starch, as a highly branched polymer. We propose that there is a relationship between the 3D printer temperature, degradation/crosslinking profile, molecular size, viscoelastic behavior, biological feature (digestive rate), and printing performance. Therefore, the main goal of the present work was to further investigate how starch macromolecules change as they undergo the above two common types of 3D printing systems, correlating these changes to the temperature during the processing, by determining the degree of starch breakdown or crosslinking. The methodology herein was to vary the main printing parameter, *i.e.*, temperature, to define the relationship between printing performance, microstructure, rheological behavior, thermal behavior, starch digestion rate, and degradation profile during the printing process.

2. Methods and materials

2.1. Materials

Normal maize starch with 10.2% moisture content, < 0.10% protein, 0.5% fat, < 1% ash, and 27% amylose content [19,20] was provided by Xinxiang Liangrun Whole Grain Food Co., Ltd. (Xinxiang, Henan, China). Dimethyl sulfoxide (DMSO) was purchased from Sigma-Aldrich (Steinheim, Germany). Para-hydroxybenzoic acid hydrazide (PAHBAH) assay (H9882, Steinheim, Germany). Isoamylase from *Pseudomonas sp.* was obtained from Megazyme International, Bray, Co. (Wicklow, Ireland). Milli-Q water was used in all instances. All other chemicals were used as received without further purification.

2.2. Pre-preparation of starch for 3D printing processes

The native starch was completely dispersed in Milli-Q water (100 g L^{-1}) at the ambient temperature and gently stirred by a magnetic stirrer for 60 min. Then, the starch suspension was sheared using a high-speed rotor-stator device (Ultra-Turrax, IKA* T25 digital, Germany) at a shear rate of 56 s^{-1} for 10 min. After completing the process, the sheared sample was collected and dried in an oven at 40 °C for 36 h. Next, the dried starch was ground to disrupt the clumps, and filtered by a sieve to attain a particle size of 30 μm.

2.3. Printing process

Before the 3D printing process, the tested starch was initially conditioned in a desiccator including a saturated potassium sulfate solution (with a relative humidity of 97%) at ambient temperature for six days to reach a moisture content of 44 g/100 g. For the printing process, three typical 3D models were designed and selected to further evaluate the printing fidelity of the starch ink. In this regard, computer-aided design software (AutoCAD; Autodesk Inc., San Rafael, CA) was used to model the lattice matrix (lattice square), pentagram, and gradient spacing (a rectangular waveform shape), which converted them to a stereolithography (.stl) file. To control XYZ direction instruction for the printers, a print path was obtained by the development of the G-code files, offered by the open-source CAM software Slic3r (slic3r.org, consulted on September 2021) from the STL (.stl) file. The extrusion printer was a micro-dispensing pump system (nScrypt-3D-450. nScrypt, Orlando, FL) equipped with a syringe pump (PHD Ultra; Harvard Apparatus Holliston, MA). The printable starch-based ink was filled with a stainless-steel container (10 mL) and stirred with a Vortex mixer (Fisher Scientific, Ontario, Canada) for 5 min, therefore eliminating any air bubbles from the ink. The nozzle tip was elevated by 1 mm upon completion of the construction of each layer and before beginning the fabrication of the subsequent layer. The extrusion printing process was performed at a temperature of 40, 70, 100, and 130 °C, and the process was continued until a proper 3D structure was printed in each case. The number of deposited layers was 8 and the width of the tip was 500 μm [21].

Regarding the LPBF method, the starch was moved to a Desktop LPBF printer (Sintratec Kit, AG, Brugg, Switzerland) to develop the 3D printed structures. A sled was used for the movement of powders in the platform reservoir (15 cm × 15 cm × 15 cm) of the printer to a building platform (15 cm × 15 cm), which provides an even and homogeneously distributed layer of powders. Before the 3D printing process, the printer was preheated to 40 °C for 30 min, offering a thorough distribution of the heated interior of the system along with the entire powder reservoir. Four different surface temperatures were selected, allowing for a surface temperature of 40, 70, 100, and 130 °C with a chamber temperature difference of 5 °C (A detailed information on the reason for selecting these surface temperatures has been provided in Section S-1 in Supplementary Materials). This shows the surface temperature of the powder bed in the building platform. The printing process was performed by the initiation of a 445 nm blue diode laser (2.3 W) with a laser scanning speed of 90 mm s^{-1}, an approximate laser spot size of 50 μm, and hatch spacing of 90 μm, which sintered the starch powders on the building platform in the particular fashion specified in accordance to the STL (.stl) model [22]. At this time, the building platform moved down, the reservoir platform moved up, and the sled distributed a thin layer of powders (layer thickness of 500 μm) on the top of the preceding layers, which was repeated layer-by-layer until the 3D structures were created. Each 3D printed structure was detached from the bed and the extra power was brushed off.

To avoid retrogradation, the 3D printed starches were immediately used for analytical and instrumental measurements. The codes of S-EXT_{40} (or S-$LPBF_{40}$), S-EXT_{70} (or S-$LPBF_{70}$), S-EXT_{100} (or S-$LPBF_{100}$), and S-EXT_{130} (or S-$LPBF_{130}$) were considered for the starch that had been extrusion (or LPBF) 3D printed at 40, 70, 100, and 130 °C, respectively. For a better interpretation of the reference and detailed printing procedures in this section, the reader is referred to the Supplementary Materials of this article (Tables S-1 and S-2).

2.4. Dissolution and debranching of starch molecules

To conduct the molecular characterization assay, the native starch or 3D printed objects (5 mg) were initially dissolved in DMSO (2 mL) including lithium bromide (0.5 wt%), which was vigorously stirred by an Ultra-Turrax (IKA* T25 digital, Germany) at 80 °C for 20 min. This step was labeled as 'Level 2′ and was performed in order to characterize the fully branched starch (whole molecules). The next step, denoted as 'level 1′, was devoted to the evaluation of separate chain branches of starch. In this phase, the 3D printed objects (10 mg) were dissolved in the prepared DMSO/lithium bromide dispersion, which was debranched using an isoamylase in acetate buffer (pH 3.5) [23]. The debranched starch dispersions were neutralized via sodium hydroxide (0.2 M) to a pH of about 7. Then, they were freeze-dried using a freeze-dryer device (Martin Christ, Alpha 1–2LD plus, Osterode, Germany) and finally dissolved again in the DMSO/lithium bromide dispersion using a magnetic stirrer for 120 min at 80 °C.

2.5. Molecular characterization by size exclusion chromatography (SEC)

The SEC separates macromolecules according to their respective corresponding hydrodynamic radius (R_h) or hydrodynamic volume (V_h). The SEC weight distributions $w(\log V_h)$ includes the whole starch ($w_{br}(\log V_h)$) or debranched starch ($w_{de}(\log V_h)$). Note that the amylopectin SEC distributions in the amylopectin are slightly degraded from the true amounts owing to shear scission in SEC [12], and therefore these whole-molecule data cannot be employed to quantify amylose content, which is instead obtained from the debranched distributions. The degree of polymerization (*DP*) of debranched starch ('Level 1′) and the average hydrodynamic radius ($\overline{R}_h$) of whole starch molecules ('Level 2′) were determined according to the procedures described in detail elsewhere [24]. Then, the molecular structures of starches were monitored through an SEC device (Agilent Technologies, Waldbronn, Germany) coupled with an isocratic pump, a series of separation columns (GRAM precolumn, GRAM 30, and 3000 analytical columns, Polymer Standard Services, Mainz, Germany), and a refractive index detector (Shimadzu RID-10A, Shimadzu Corp., Kyoto, Japan). The mobile phase was DMSO containing 0.5% (w/w) lithium bromide solution, which was filtered with a hydrophilic Teflon membrane filter (0.2 μm pore size and 47 μm diameter, Millipore Billerica, MA). The separation column was kept at 80 °C and the detector was set at 48 °C. The flow rate was also adjusted at 0.6 mL min^{-1}. Each injected starch was obtained with a level of 5 mg mL^{-1} in the identical eluent. A series of pullulan standards (Polymer Standard Services, Mainz, Germany) with different molecular weights ranging from 0.342 to 1,6600 kDa was utilized for calibration. Each pullulan standard (2 mg) was dissolved in the DMSO/lithium bromide solution (2 mL) with a magnetic stirrer for 150 min at 80 °C. The Mark–Houwink parameters for this eluent at 80 °C are $K = 2.424 \times 10^{-4}$ d Lg^{-1} and $\alpha = 0.68$ [12]. For convenience, the results of hydrodynamic volume (V_h) are presented in terms of hydrodynamic radius (R_h), calculated as follows:

$$V_h = 4/3\ \pi\ R_h^3 \tag{1}$$

Each SEC chromatogram was evaluated by PSS WINGPC Unity Software (PSS Polymer Standards Service GmbH, Mainz, Germany), normalizing to obtain a similar amylopectin peak height. The detector signal provides the size distribution values ($w(\log V_h)$), which were plotted against *DP* or log R_h [12]. This offers the size distribution as a function of hydrodynamic volume or hydrodynamic radius, which is a molecular quantity independent of SEC set-up. This also allows the resulting data to be reproduced, while it is inappropriate to present such data as elugrams (in terms of volume or elution time, which is a molecular quantity) since the elution changes with the particular SEC set-up, and even from day to day with a specific circumstance.

2.6. Dynamic oscillatory rheological measurement

An AR-G2 rheometer (TA Instruments, West Sussex, UK) coupled with a heating circulator (Julabo, F-12, Seelbach, Germany) was used to detect the dynamic rheological measurements of printed samples at 25 °C. A cone and plate geometry (60 mm diameter, 2° cone angle, and 58 µm gap) was utilized for the experiment. Initially, the limit of the linear viscoelastic region (*LVR*) was detected by a strain sweep measurement (0.01–100%, 1.0 Hz). According to our previous publications [2,3], the critical strain for each sample was calculated to be the strain at which the storage modulus (G') deviated by more than 5% from its low strain plateau value. Then, the frequency sweep evaluations were performed at 50% of the smallest critical strain determined (1.0%) to ensure that all tests were carried out within the *LVR*. After that, the frequency sweep assay (0.1–100 Hz) of printed samples was performed within the *LVR*. The rheological parameters including G', loss modulus (G''), loss tangent (tan δ), and complex viscosity (η^*) were obtained from the manufacturer's supplied (TRIOS, TA Instruments, West Sussex, UK) computer software [3].

2.7. Molecular dynamics by nuclear magnetic resonance (NMR)

The proton mobilities of native starch and 3D printed structures were evaluated through a low-field pulsed ^{1}H NMR spectrometer (MiniSpec mq 20 TD, Bruker, Rheinstetten, Germany) with a resonance frequency of 20 kHz and a strength of 0.47 T. The proton distributions were obtained with a free induction decay (FID) with a single 90° pulse and an acquisition period of 0.5 ms. Moreover, a Carr-Purcell-Meiboom-Gill (CPMG) pulse sequence was used with a pulse separation between the 90° and 180° pulse of 0.1 ms. For both measurements, a recycle delay of 3 s was used with 32 accumulated scans to enhance the signal-to-noise proportion. The pulse lengths of the 90° and 180° pulse were 2.80 and 5.56 µs, respectively. The number of collected data points was 500 and 2500 for the FID and CPMG sequence, respectively. The inverse Laplace transforms were used by the CONTIN algorithm to convert the transverse relaxation curves into continuous distributions of T_2 relaxation times. The region of each proton population is proportional to the relative extents, expressed in arbitrary units normalized per gram of sample (wet basis). In the NMR result section, where the distribution curves are presented, a characteristic continuous proton distribution of the triplicate measurements was designated. FID measurements determined the less mobile proton populations, whereas more mobile protons were analyzed by the CPMG pulse sequence [25,26].

2.8. Thermal behavior by differential scanning calorimetry

A differential scanning calorimeter (DSC-60, Shimadzu, Kyoto, Japan) was used to monitor the thermal properties of native starch and 3D printed samples. The 3D printed starches with a ratio of 0.33 g/100 g (dry basis/water) were dispersed in Milli-Q water. Following this, the samples (approximately 10 mg) were transferred to a hermetically sealed aluminum pan and conditioned overnight before the test. Then, they were heated from -5 to 145 °C at a temperature increase rate of 10 °C min^{-1}. The experiment was performed in a nitrogen atmosphere (54 psi) with a sensitivity of 0.2 µ W [27,28].

2.9. X-ray diffraction (XRD)

An X-ray diffraction device (XRD, Philips X-Pert PRO, Netherlands) was employed to detect the XRD pattern and relative crystallinity degree (*RCD*) of native starch and 3D printed objects. The device was set up to 40 kV energy, 30 mA current, and Cu Kα irradiation ($\lambda = 1.54056$ Å). At first, each sample was conditioned in a desiccator including a saturated NaCl solution (relative humidity of 75.1%) at 25 °C for two days to reach a moisture content of 14.1 g/100 g. Next, they were irradiated in the range of 3–44° and scanned at a speed of 0.018°/min at room temperature. To measure *RCD*, the total area (I_t) and the area under XRD peaks (I_p) were obtained via the software supplied by the manufacturer (EVA, Version 9.0), and the *RCD* was determined by the following equation [26]:

$$\text{RCD}\ (\%) = (I_p/I_t) \times 100 \tag{2}$$

2.10. In vitro starch digestion and first-order kinetics

The native starch or 3D printed samples (0.1 g, w/w%) were incubated in phosphate-buffered saline (20 mL) with 3.9 units of α-amylase at 37 °C with gentle mixing (a rotation speed of 400 rpm) for 100 min. At time intervals up to 100 min, 0.3 mL of aliquot was blended with 0.3 mL ice-cold sodium carbonate solution (0.4 M) to stop the reaction. Following that, it was centrifuged (Eppendorf centrifuge 5417 R, Hamburg, Germany) at 1409 G-force in the ambient condition for 5 min to eliminate the undigested starches [29]. The amounts of reducing sugar (maltose equivalent) in the supernatant were measured by the PAHBAH test [30]. The reducing sugar released was determined using the following equation:

$$\text{Maltose equivalent } \mathit{released}\ (\%) = Wm/Ws \tag{3}$$

where *Wm* is the total weight of maltose equivalent to supernatant and *Ws* is the dry weight of sugar.

The undigested starch residues were collected as precipitates after centrifugation. These were washed twice with de-ionized water, and then freeze-dried for further structural analysis. The reducing sugar profile or digestogram was then fitted to a first-order reaction equation (using the log of slope (LOS) plots) for the starch digestion kinetics as follows:

$$\text{In}\left(\frac{dc}{dt}\right) = \text{In}(\text{C}_\infty \text{k}) - \text{kt} \tag{4}$$

Here *t* is digestion time, *C* is digested starch at the incubation time *t*, C_∞ is digestion at infinite time, and *k* is the reaction rate constant. The rate constant is a function of the fixed amylase and starch concentrations used in the digestion. Therefore, it should be noted that this is a *pseudo*-first-order reaction, to be more precise [29].

2.11. Pasting features

The pasting properties of native starch or 3D printed structures were assessed by a Rapid Visco-Analyzer (RVA-4, Newport Scientific, Australia). Each 3D printed structure (4.0 g) was mixed with water (30.0 mL) and placed in an RVA container. The samples were pre-sheared with the rotation speed of the plastic paddle set to 900 rpm for 25 s [31]. Next, the samples were stirred at the rotation speed of 150 rpm and maintained at 45 °C for 60 s and heated to 95 °C at a rate of 5 °C min^{-1} afterward held at 95 °C for 5 min. The cooling step was achieved with a rate of 5 °C min^{-1} to 45 °C and was finally held at 45 °C for 5 min

2.12. Printing performance measurement

Each 3D printed object was transferred into a specific chamber (20 cm × 20 cm × 20 cm) to be photographed using a digital camera (α 7M3 E-Mount, Full-Frame Mirrorless, 24.2 MP, Sony, Tokyo, Japan) [32].

2.13. Morphological observation by FE-SEM

The morphological structure and integrity of the 3D printed objects were captured through a field-emission scanning electron microscope (FESEM Carl Zeiss Supra 50VP, Oberkochen, Germany). The specimens were sputtered with a 2-nm layer of gold for 60 s (SPI supplies, West Chester, PA) to avoid electrical charging. A back-scattered electron mode was used for the SEM observation. A 5 kV energy level was applied to prevent the 3D structures from being damaged with a magnification of 20.00 kX.

2.14. Statistical analysis

All instrumental experiments were carried out in triplicate with the mean and standard deviation of the data calculated and reported. Analysis of variance (ANOVA) was utilized for the determination of the main effects and to examine the independence or the interactions between various factors on the instrumental and sensory data. Duncan's multiple range test was applied to separate means of data when significant differences ($P < 0.05$) were observed.

3. Results and discussion

3.1. Changes in molecular behavior by SEC

The SEC is an efficient technique to monitor degradation or cross-linking reactions of biomacromolecules [12]. Concerning starch as a highly branched polymer, it was reported that only its short-chain branching (amylopectin) is strongly influenced by processing (e.g., extrusion) [12,33]. This is likely because the chains in this fraction are not able to easily align with each other under high shear, due to its many side chains [33]. According to SEC, the short-chain branching parts tend to degrade more towards the internal area instead of those adjacent to the exterior regions of the molecule. In the current work, different structural levels of starch were evaluated under variable temperature conditions of extrusion or LPBF 3D printing process. It was shown that starch has some specific benefits aimed at the drives of mechanistic investigation, as the molecular weight distribution of separate chains is readily attained via the addition of a debranching enzyme. This quantitatively degrades the branch areas entirely [12]. Fig. 1 shows the SEC weight distributions for the debranched (Level 1) and whole (Level 2) starch molecules, which were normalized to obtain a similar height for the highest peaks. The SEC weight distributions of $w(\log V_h)$ were plotted as a function of the degree of polymerization (*DP*) (debranched starch) or hydrodynamic radius (whole starch molecule). As illustrated in Figs. 1a and 1c, a typical bimodal peak, related to the amylopectin chains (short-chain branching), was observed for a *DP X* lower than 100, while an SEC weight distribution of the debranched starch (Level 1) was detected with a wider bimodal peak attributed to the amylose branches ($DP\ X > 100$) [34]. Figs. 1b and 1d also present the SEC weight distribution of whole starch (Level 2), which illustrates the usual feature of the amylose peak with 5 nm $< R_h <$ 200 nm and the amylopectin peak with larger molecular sizes of 200 $< R_h <$ 2000 nm [12,33].

Compared to native (non-printed) starch, the SEC weight distributions of debranched starch were qualitatively unchanged by the extrusion 3D printing process (Fig. 1a). Regarding SEC weight distributions of fully branched starch (whole starch), there was a reduction in the peak area of amylopectin after 3D printing compared with its native counterpart (Fig. 1b). In this case, the peak area of the amylose component was mostly retained. It is well known that amylopectin is more sensitive to degradation through extrusion shearing force as compared to amylose

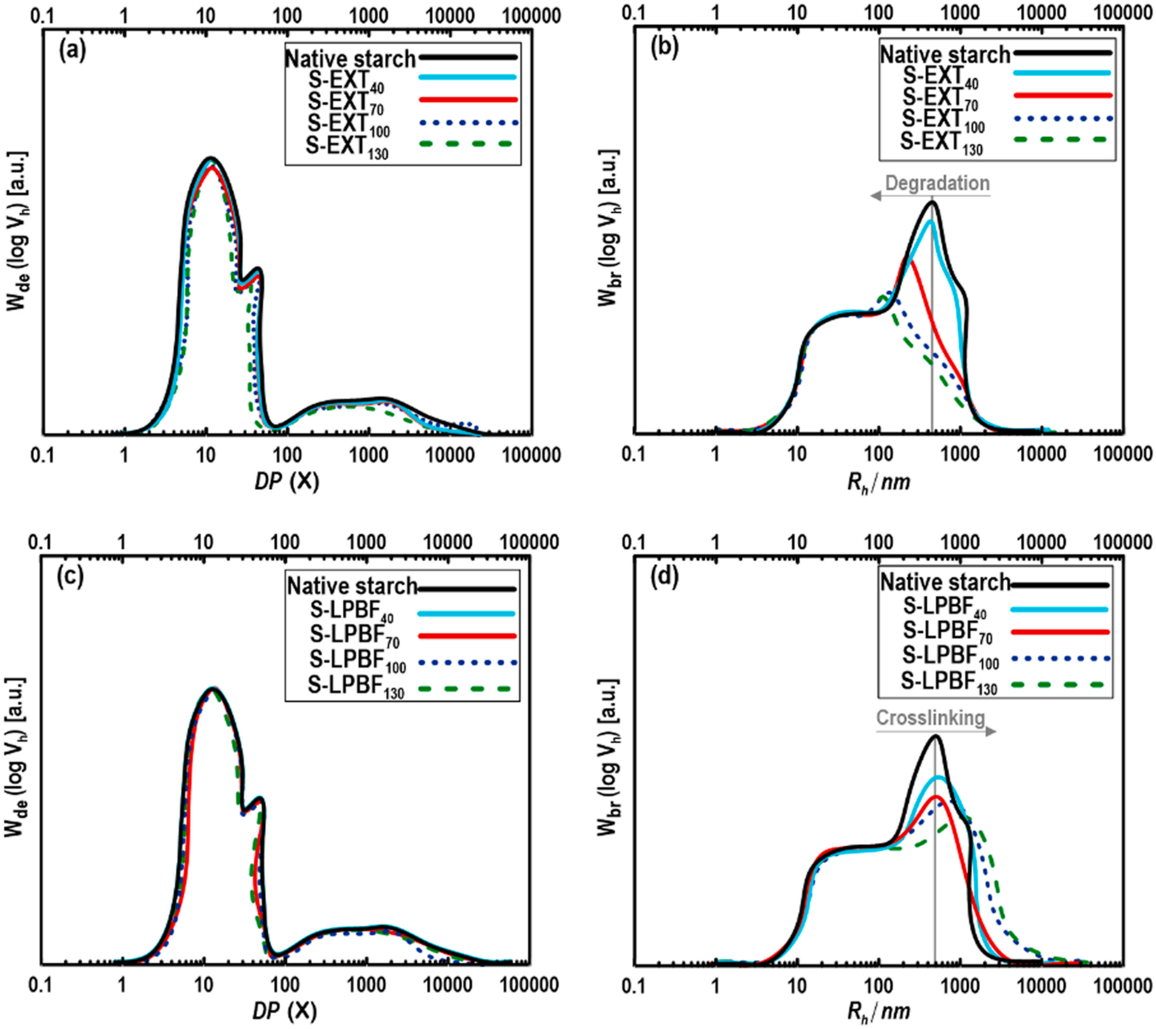

Fig. 1. (a,c): SEC weight distributions of debranched native or 3D printed starches (Level 1). (b,d): SEC weight distributions of whole native or 3D printed starches (Level 2).

[12,33,34]. This indicates that the glycosidic linkages nearby or at the building blocks (branching points) of amylopectin are susceptible to shear cleavage due to its large molecular size and comparatively inflexible structure. Though, in the current work, there was not sufficient information to make the deduction that any specific building blocks are more prone to shear degradation when subjected to extrusion in the 3D printing process, than any others with complete certainty. It was reported that there could be a decrease in the entire size of the starch molecule with the depolymerization of only a small number of amylopectin chains [35].

Concerning LPBF 3D printing, the SEC weight distributions of native starch showed that the amylopectin peak unchanged in the debranched starches (Fig. 1c), but declined in the whole starch molecules (Fig. 1d) after the printing process. As reported in the literature, the LPBF could develop a crosslinked network inside the polymeric backbones [9,11,14], however, its mechanism awaits further study. LPBF melts the solid polymer to a liquid phase under the CO_2 laser, which can lead to (*i*) an increase in the molecular size/weight caused by crosslinking/branching of molecular chain, and (*ii*) development of large particles formed from aggregated of smaller pieces [7,9,11].

To quantify the molecular behavior of starch under extrusion or LPBF 3D printing techniques, the average hydrodynamic radius ($\overline{R}_h$) and hydrodynamic radius (R_h) values at the main peak maximum (or the middle of a smaller peak) were measured through the SEC weight distributions of fully branched starch (*i.e.*, Level 2) (Table 1). Each 3D printing process had different impacts on both $\overline{R}_h$ and R_h values at the main peak maximum. With an increasing temperature of extrusion 3D printing from 70 °C to 130 °C the $\overline{R}_h$ value of the amylopectin peak became smaller ($P < 0.05$). However, there was no significant difference between $\overline{R}_h$ value of native starch or starch printed at 40 °C ($P > 0.05$). Moreover, the R_h value at the main peak maximum for the 3D printed starches processed at 100 and 130 °C seemed to have a lesser extent (32–41 nm) in comparison with that printed at 70 °C (212 nm) (Table 1). The degree of polymerization distribution of separate branches in the starch is simply attained through the action of the debranching enzymes along with the fact that there was no reaction during the extrusion printing process, excluding simple chain degradation, thus supporting the mechanistic interpretation [12,33]. During extrusion 3D printing, the huge deformation and shearing forces can cleave the hydrogen bonds along the starch backbone and degrade these linkages, thus disrupting the polymer structure [12].

Table 1
Structural features of starch extrudates from different processing conditions detected by SEC measurement.

Sample type	$\overline{R}_h$ (nm)	R_h (nm) at peak maximum		Crystallinity (%)	V-type crystallinity (%)
		Main peak	Smaller peak		
Native starch	107 ± 2^c	496 ± 4^e	49 ± 1^a	44 ± 2^h	Trace
S-EXT$_{40}$	106 ± 3^c	387 ± 5^d	49 ± 2^a	36 ± 1^f	Trace
S-EXT$_{70}$	104 ± 4^c	212 ± 4^c	52 ± 1^b	11 + 1^a	8
S-EXT$_{100}$	41 ± 2^b	143 ± 3^b	50 ± 1^a	13 ± 1^b	10
S-EXT$_{130}$	32 ± 3^a	118 ± 2^a	49 ± 1^a	15 ± 1^c	10
S-LPBF$_{40}$	105 ± 6^c	536 ± 5^f	52 ± 1^b	39 ± 2^g	nd*
S-LPBF$_{70}$	105 ± 6^c	561 ± 4^g	49 ± 2^a	34 ± 1^e	nd
S-LPBF$_{100}$	116 ± 3^d	704 ± 8^h	49 ± 1^a	34 ± 1^e	nd
S-LPBF$_{130}$	121 ± 4^e	1244 ± 11^i	52 ± 1^b	30 ± 1^d	nd

[a–i] Means (three replicates) within each column with different letters are significantly different ($P < 0.05$), Duncan's test.
*Not detected.

In relation to the LPBF 3D printing process, the R_h value at the main peak of 3D printed starches, sintered at all temperatures, appeared broader (536–1244 nm) compared to native starch (Table 1). The SEC data obtained for LPBF printing highlighted that the starch can be considered a reactive compound as explained by an increase of the molecular size, possibly due to the development of inter- and intramolecular linkages. This shows a crosslinking reaction could rationally take place in the LPBF 3D printed starches. In conclusion, the results already show that the starch was more degraded upon extrusion 3D printing, whereas it tended to produce a crosslinked network during the LPBF process, with a maximum stable size recognizable after the LPBF 3D printing.

3.2. *Viscoelastic evaluation by frequency sweep*

Mechanical strength is a principal physical feature that relates closely to the degradability or stability of a 3D printed structure [2,36]. The viscoelastic properties of all the produced 3D printed samples were obtained using the frequency sweep test and their mechanical spectra are presented in Fig. 2. Regardless of the sample type, the $G'(\omega)$ and $G''(\omega)$ moduli both increased with increasing frequency (0.1–100 Hz), with $G'(\omega)$ remaining higher than $G''(\omega)$ at any frequency. This suggests that all the 3D printed samples showed a quasi-solid behavior with a gel-like structure [2]. With regard to the temperature of extrusion printing, the $G'(\omega)$ and $G''(\omega)$ moduli of 3D printed samples showed an increasing trend up to 70 °C and then decreased, which is likely associated with the difference in the starch structure (Fig. 2a). At the lower extrusion printing temperature (40 °C), there was the presence of intact and unbroken granules in the system. As the temperature increases to 70 °C (assigned to gelatinization temperature), there is an enhancement of collision between swollen granules, as well as increasing motion of starch chains. Thus, the starch system was strengthened. Following the extrusion printing at a temperature higher than gelatinization of starch, $G'(\omega)$ and $G''(\omega)$ moduli of starch decreased, but still retained the dominance of elastic character throughout all frequencies (Fig. 2a). It was shown that the macromolecules are susceptible to shear depolymerization while printing, where the polymeric chains are thermomechanically degraded [6]. In the current study, this was noted particularly at the higher printer temperatures during extrusion, since the viscoelastic moduli tended to decrease with increasing temperature, owing to a greater scission of the biopolymeric chains. At the higher temperatures, the mobility of starch chains is increased, making the chain interactions less dominant, and accordingly resulting in weakened strength.

In the case of LPBF 3D printing, the viscoelastic moduli of the native starch were also increased when a surface temperature of 70 °C was applied and then decreased with the domination of elastic modulus over the viscous parameter throughout the frequency sweep test (Fig. 2d). Compared to extrusion 3D printing, the viscoelastic moduli of LPBF printed starches showed higher values. This demonstrates the development of the high elastic or gel-like character of these printed samples. The higher viscoelastic moduli of LPBF 3D printed samples when compared to extrusion printing might be the result of chain crosslinking/branching, which led to the formation of a stronger gel network. It has been reported that a rise in the viscoelastic parameters after LPBF 3D printing may indeed arise from crosslinking or post-condensation [10].

In general, the frequency sweep measurement considers the response of the structure of the biomaterial to different characteristic time intervals: a moderately low frequency (*i.e.*, 1 Hz) considers the response over a long time (1 s) in comparison with a relatively high frequency (*i.e.*, 10^2 Hz) that could probe the response to external stress at a short time (10^{-2} s) [2]. Bonds between chains/particles in a macromolecule could be degraded or formed during a given time, either spontaneously or

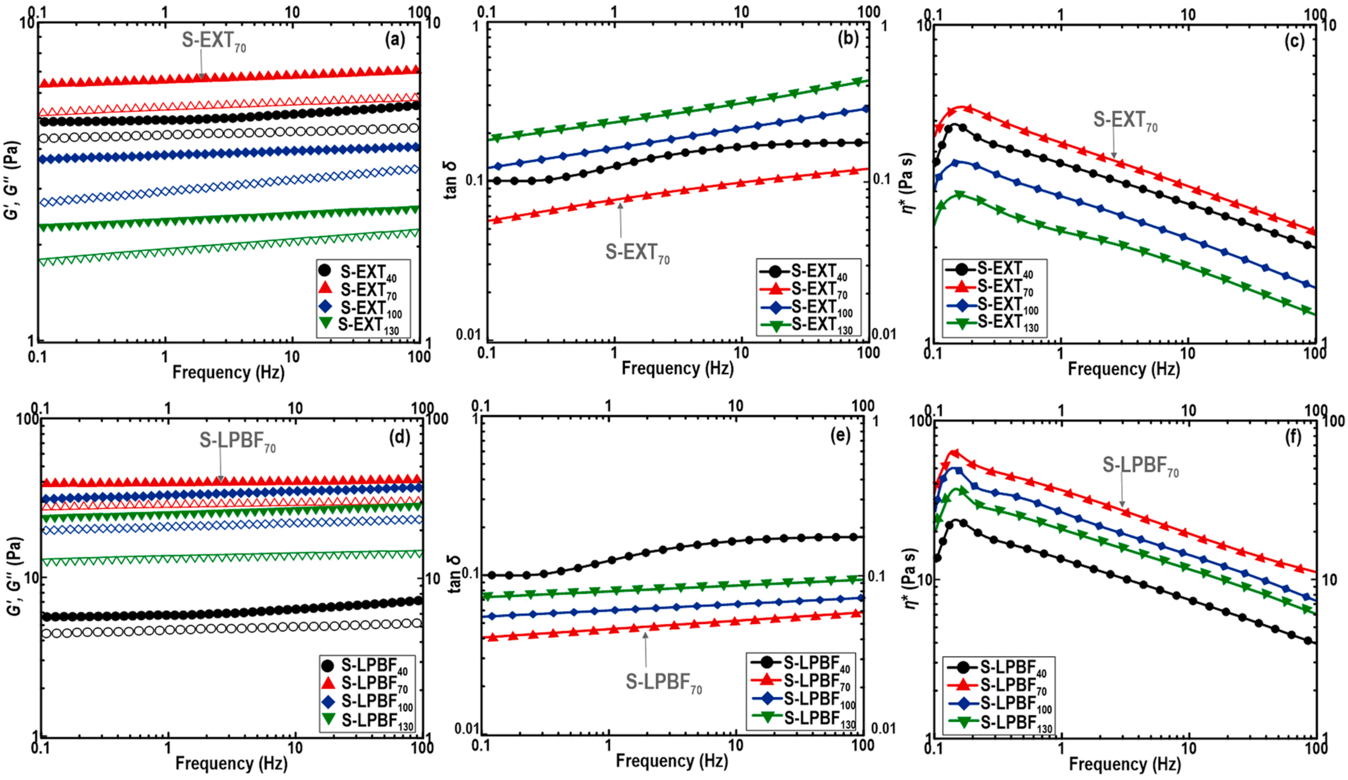

Fig. 2. Changes in the dynamic moduli of native starch, printed by extrusion (a) and LPBF (d) 3D printing systems, as a function of frequency, where elastic modulus, G', is solid symbols and loss modulus, G'', is open symbols. Changes in tan δ of native starch, processed with extrusion (b) and LPBF (e) 3D printing processes, as a function of frequency. Changes in η^* of native starch, printed by extrusion (c) and LPBF (f) 3D printing systems, as a function of frequency.

resulting from applied forces. Deformation/reformation of the linkages causes a structural alteration, hence affecting the mechanical strength [37]. With regard to the extrusion 3D printed samples, the slope of G' (ω) slightly increased as a function of oscillatory frequency, while G'' (ω) values showed a higher frequency dependence and increased with a greater slope (Fig. 2a). In contrast, the slope of G' (ω) and G'' (ω) moduli concerning the LPBF 3D printed samples showed a similar slight increase as a function of frequency (Fig. 2d). These observations can be confirmed by evaluating the extent of tan δ (G''/G') (Figs. 2b and 2e), which was changed by increasing the frequency without being 1 (or >1) regarding all samples. A high dependency of the tan δ to frequency changes was detected for the extrusion 3D printed samples (Fig. 2b), representing a tendency toward a more viscous liquid character at a higher oscillatory frequency. Compared to the extrusion printed starches, the improvement of G' (ω) (Fig. 2d) of LPBF printed starches followed by a less dependency of tan δ on the frequency (Fig. 2e) may suggest the development of a longer lifetime of intermolecular connectives, more stable molecular structure, along with a greater recoverability upon oscillation. These results are in accordance with the complex viscosity (η^*) data (Figs. 2c and 2f). In this case, the η^* values were reduced approximately linearly as a function of frequency. For extrusion 3D printing, the η^* values were, first, increased up to 70 °C (due to starch gelatinization), and then decreased after starch printing in a temperature range of 100–130 °C. This suggests that extrusion 3D printing induced deterioration of the structure of 3D printed starches, with the development of a less structured and hence a weaker network. In contrast to extrusion printed starches, the η^* values were increased as the starch was printed by the LPBF technique, especially when it was treated at a surface temperature of 70–130 °C. This implies a lower molecular motion in the matrix caused by a greater amount of inter-chain connectivity. One of the reasons for this result could be associated with the development of newly crosslinked networks generated by the LPBF printing system, which could increase the viscoelastic behavior of starch. Contrary, the shear degradation of the biopolymeric chains upon extrusion printing causes the loss of a more elastic gel-like character.

3.3. *Proton mobility*

The state and amount of water have a significant effect on the physical and structural properties of the 3D printed structures [25,26]**.** A relationship between molecular mobility of macromolecules and water-induced macroscopic processes, including changes in crystallinity and system rigidity, can be analyzed by low-field pulsed ^{1}H NMR [25]. In this case, the free induction decay (FID) and Carr-Purcell-Meiboom-Gill (CPMG) proton distribution curves of 3D printed starch variants are depicted in Fig. 3 and the obtained relaxation times (T_2) are summarized in Table 2. There are two characteristic FID and three CPMG proton populations in all samples, denoting these as $t_{(2,1)}$, $t_{(2,2)}$, $t_{(2,3)}$, $t_{(2,4)}$, and $t_{(2,5)}$, labeled from the shortest to the longest relaxation time, respectively. In the case of native starch, the $t_{(2,1)}$ with the lowest proton mobility (T_2=0.029 ms) was detected in the FID population. This population is mainly comprised of the rigid non-exchanging CH protons of amylopectin crystals and densely packed amorphous starch, which are not exposed to water (tightly bounded water) [26]. The $t_{(2,2)}$ population, located at the FID sequence (T_2=0.057 ms), could be associated with CH protons of amorphous starch that have modest contact with confined water. The $t_{(2,3)}$ population, located at the CPMG spectrum (T_2=3.96 ms), relates to the hydroxyl protons of water and/or intragranular exchanging protons of starch in a less mobile environment. It could rationally be assumed that the rigid non-exchanging CH protons of starch are part of this panel [25, 26]. The $t_{(2,4)}$ panel, as the second dominant proton population, was distinguished in the CPMG sequence and is associated with the more mobile hydroxyl protons of starch possessing strong interaction with water (T_2=88.8 ms). The last proton population, specified as $t_{(2,5)}$ and

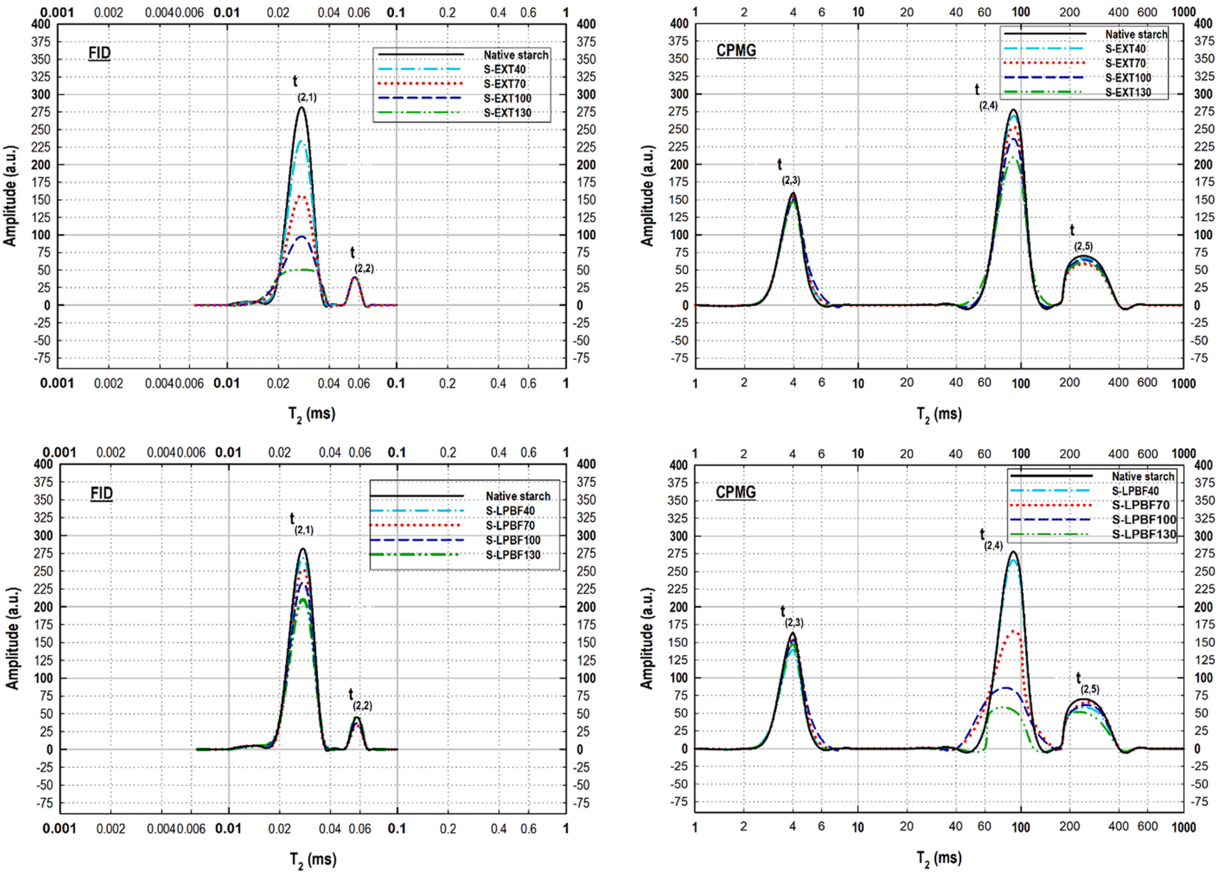

Fig. 3. NMR proton distributions of extrusion (top graphs) and LPBF (bottom graphs) 3D printed starches obtained from inverse Laplace transformation of the FID and the CPMG pulse sequences.

Table 2
A summary of relaxation time of signal amplitude of protons in the starch treated by extrusion and LPBF 3D printing processes.

Printer/Surface temperature (°C)	$t_{(2,1)}$ (ms) × 10^{-3}		$t_{(2,2)}$ (ms) × 10^{-3}		$t_{(2,3)}$ (ms)		$t_{(2,4)}$ (ms)		$t_{(2,5)}$ (ms)	
	Extrusion	LPBF	Extrusion	LPBF	Extrusion	LPBF	Extrusion	LPBF	Extrusion	LPBF
- (Native)	29 ± 1^a	29 ± 1^a	57 ± 2^a	57 ± 2^a	3.96 ± 0.12^c	3.96 ± 0.12^c	88.8 ± 1.3^a	88.8 ± 1.3^c	248 ± 4^b	248 ± 4^c
40	29 ± 1^a	29 ± 2^a	56 ± 1^a	57 ± 1^a	3.91 ± 0.11^a	3.92 ± 0.16^b	88.9 ± 1.4^a	88.6 ± 1.3^c	248 ± 4^b	250 ± 3^c
70	29 ± 2^a	28 ± 1^a	56 ± 1^a	57 ± 1^a	3.93 ± 0.07^b	3.95 ± 0.18^c	88.1 ± 1.8^a	87.2 ± 1.0^c	249 ± 5^b	251 ± 3^c
100	28 ± 2^a	28 ± 1^a	56 ± 2^a	56 ± 2^a	3.92 ± 0.10^a	3.93 ± 0.17^b	88.7 ± 2.1^a	75.3 ± 1.3^b	240 ± 3^a	247 ± 2^b
130	28 ± 1^a	27 ± 1^a	57 ± 1^a	56 ± 1^a	3.90 ± 0.15^a	3.89 ± 0.19^a	88.0 ± 2.0^a	69.7 ± 1.1^a	247 ± 3^b	242 ± 3^a

[a–e] Values are the average of triplicates ± standard deviation. Different superscripts in each column show a significant statistical difference ($P < 0.05$).

having the highest mobility (T_2=248 ms), appeared on the CPMG sequence. This likely arises from the relaxation signals of lipid in the starch [25].

As visualized in Fig. 3, there is some difference in the NMR pattern between the starch treated by 3D extrusion and LPBF printing systems regarding the $t_{(2,1)}$ panel (containing the tightly bounded water). In this case, the amplitude of $t_{(2,1)}$ was considerably reduced after extrusion 3D printing with a pronounced effect seen at the higher printer temperatures. The LPBF printing process, especially its higher surface temperatures, also led to a decrease in the $t_{(2,1)}$ peak area, albeit the reduction was lower than extrusion 3D printing. These results also agree well with those obtained by SEC weight distributions. The further decline in the peak area of $t_{(2,1)}$, observed for extruded 3D printed starches, is possibly associated with a notable decrease in the starch crystalline area due to fragmentation and disintegration of amylopectin fraction. Therefore, the extrusion printing can further reduce the gelatinization temperature compared to LPBF printing, and consequently starch swelling. The presence of a linear correlation between the peak intensity of the $t_{(2,1)}$ population and the crystallinity of a system has also been demonstrated in the literature [25,26].

In contrast to $t_{(2,1)}$, the proton populations of $t_{(2,2)}$ and $t_{(2,3)}$ were qualitatively unchanged following both 3D printing processes when compared with those of the native (non-printed) starch. However, a decrease was detected for the amplitude of $t_{(2,4)}$ (associated with free water) following both extrusion and LPBF printing processes. In this case, the intensity of the $t_{(2,4)}$ peak was much more reduced after LPBF printing compared to extrusion 3D printing. The much lower amplitude of the $t_{(2,4)}$ panel in the LPBF printed starches is likely to be due to a reduced portion of more mobile amorphous starch that is strongly interacting with water. This may show that a new crystalline structure in the amorphous domains of starch was developed as a result of cross-linking/branching upon LPBF 3D printing.

Another interesting result obtained in this study concerned (spin-spin) relaxation time, where the LPBF printing system exerted an important change in the T_2 of the $t_{(2,4)}$ population (Table 2). The NMR data revealed that the T_2 relaxation time of the $t_{(2,4)}$ population shifted to a shorter relaxation time after LPBF 3D printing. As mentioned above, this panel comprises mobile hydroxyl protons of water in the intergranular space, which are in exchange with hydroxyl protons of starch on the granular surface. This result reveals a mobility reduction in the exchanging hydroxyl protons of starch and those of water after LPBF 3D printing. It has been stated that a decrease in the relaxation times of the $t_{(2,4)}$ panel signifies an increase in the stiffness of the system [26]. The reduced mobility of the $t_{(2,4)}$ population for LPBF printed starches was most possibly resulting from the strengthening of the 3D structural network due to crosslinking/branching. This further highlights a positive correlation between the system hardness and the T_2 relaxation time of the $t_{(2,4)}$ panel.

3.4. *Thermal behavior*

Figs. 4a and 4b show the DSC thermograms of starch as influenced by extrusion or LPBF printing systems at the different printer or surface temperatures. Two characteristic peaks were observed in the thermograms of native and 3D printed starches. Concerning the native starch, the first endothermic behavior showed a peak temperature (Tp_1) at about 72 °C with an enthalpy (ΔH_1) of 11.09 J g^{-1}, which could be assumed to be the melting of the starch crystalline domains (*i.e.*, gelatinization temperature peak) [27]. The second peak, with a peak temperature (Tp_2) of 130 °C and an enthalpy (ΔH_2) of 2.12 J g^{-1} could be assigned to the melting of the amylose-lipid complexes [27].

The thermal behavior of extrusion or LPBF printed starches displayed noticeable differences in terms of position or enthalpy of the endothermic peak. These variations are principally associated with the difference in the melting peak of starch crystalline regions (*i.e.*, the first order-disorder transition of the amylopectin peak) (Figs. 4a and 4b). Regarding extrusion 3D printed starches, the gelatinization temperature peak was shifted to the lower temperatures following the printing process. Compared to native starch, the Tp_1 of the 3D printed sample treated at 100 °C (*i.e.*, S-EXT$_{100}$) was reduced by a noticeable amount to a temperature of 68 °C. There was a similar decrease seen for the starch printed at 130 °C (*i.e.*, S-EXT$_{130}$), where the Tp_1 peak was found to occur at about 62 °C. According to the literature, the melting peak of crystalline starch is reduced to a lower temperature as a result of extrusion

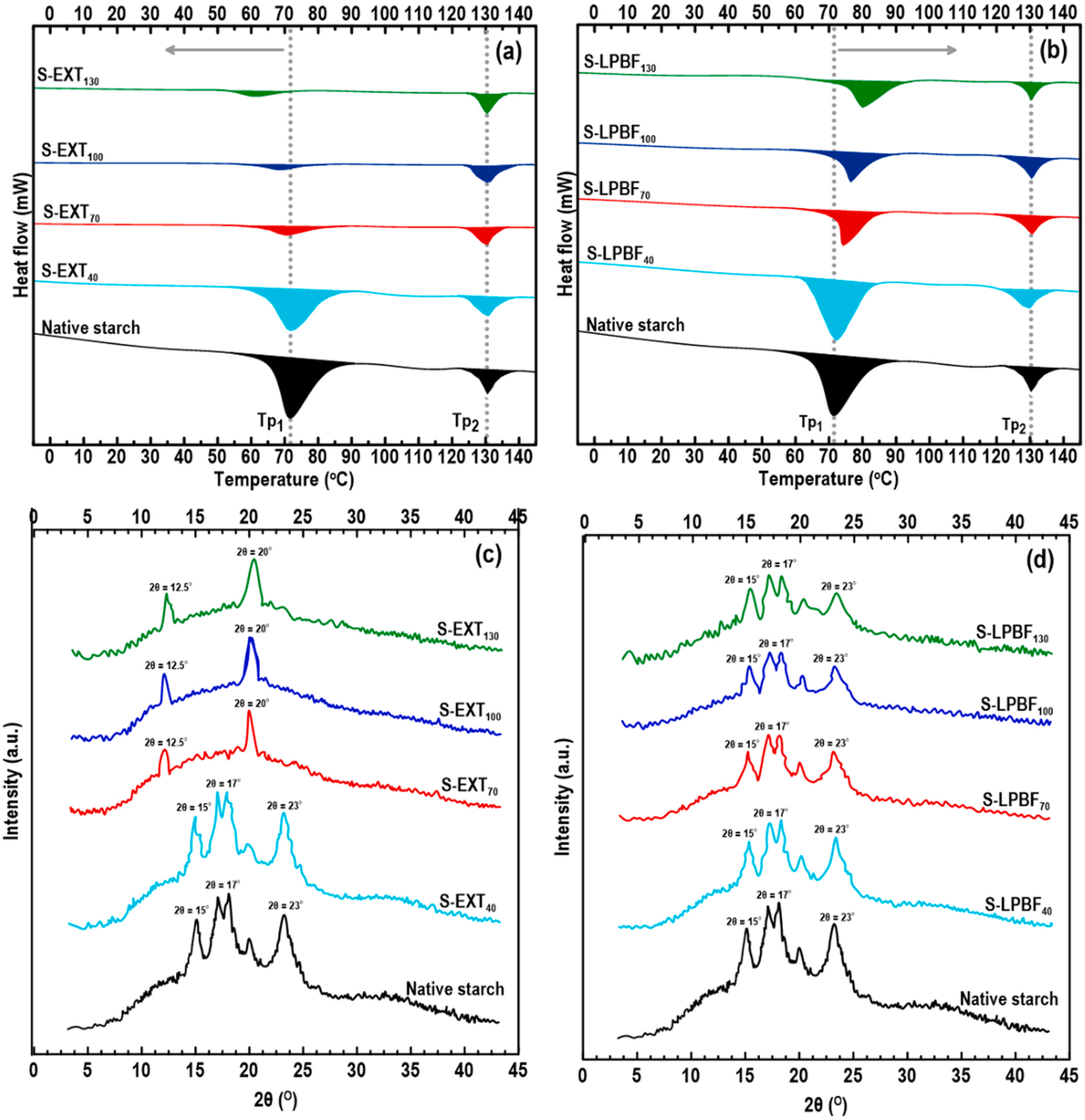

Fig. 4. DCS thermograms (a,b) and XRD patterns (c,d) of starch processed with different printer temperatures of extrusion or surface temperatures of LPBF 3D printing systems.

shearing force because of the fragmentation and disintegration of starch structures [27]. In accordance with this result, NMR data revealed that the extrusion 3D printing reduced the non-exchanging protons of amylopectin crystals. There is also a similar result obtained by SEC weight distributions. In contrast, a totally different trend was detected concerning the LPBF 3D printed starches, where the melting peak of crystalline starch was shifted to higher temperatures. This was especially the case at the higher surface temperatures of the printing process (Fig. 4b). A similar thermal behavior, regarding some synthetic polymers processed with an LPBF 3D printer, has also been reported in the literature [10]. A considerable increase in the transition of the amylopectin peak after LPBF 3D printing is likely because of the development of a crosslinked network inside the molecular backbones. Consequently, this aids the formation of a particular hydrogel network upon heating. Thus, good structural stability and high resistance against temperature rise cause the system requires a higher temperature for disorganization/melting [27].

The changes in the enthalpy of the endothermic peak as affected by both printing processes were also evaluated. As Fig. 4a indicates, there was a prominent reduction in the enthalpy of the first endothermic peak (the first order-disorder transition of the amylopectin peak) regarding the extrusion 3D printed starches, where the peak area of S-EXT$_{70}$, S-EXT$_{100}$, and S-EXT$_{130}$ dropped to a value of 1.89, 1.22, and 1.03 J g^{-1}, respectively. Regardless of the role of extrusion force, the applied temperature (above 70 °C) during the extrusion 3D printer can change the double-helical structures of the crystalline region (amylopectin). This could lead to a notable decrease in the starch crystallinity; thus, the system requires less energy to be gelatinized. Similarly, there was a decrease in the enthalpy of the amylopectin peak after LPBF 3D printing (Fig. 4b), however, its reduction was lower than extrusion 3D printing. In this case, the enthalpy of S-LPBF$_{70}$, S-LPBF$_{100}$, and S-LPBF$_{130}$ reduced to a value of 8.91, 8.57, and 8.17 J g^{-1}, respectively. This indicates that the crystalline area of starch was slightly affected by LPBF 3D. As mentioned earlier, the LPBF 3D printing process may induce some levels of crosslinking/branching between the biopolymeric chains at the molecular level. It is important to note that there was no important difference regarding the enthalpy peak of the amylose-lipid complexes in both extrusion and LPBF 3D printing processes (the second endothermic peaks). This is because these molecules are sufficiently small to be stable against shear degradation or fusion under both printing conditions.

3.5. *Crystalline evaluation*

The XRD measurement was performed to track the effectiveness of different printer/surface temperatures of extrusion or LPBF printing systems on starch crystalline structure (Figs. 4c and 4d). The X-ray diffractogram of native starch showed various typical reflections around $2\theta = 15^\circ$ (d_{001}=5.3 Å), $2\theta = 17^\circ$ (d_{001}=4.9 Å), and $2\theta = 23^\circ$ (d_{001}=4.4 Å) with a relative crystallinity degree (*RCD*) of 43%. The observed pattern proposes a characteristic A-type crystalline packing arrangement inside the starch granules. As Fig. 4c presented, there is no substantial change in the XRD pattern of S-EXT$_{40}$ (*RCD*=~43%). In contrast, the intensities of starch diffraction peaks were detected to be considerably reduced for S-EXT$_{70}$ (*RCD*=~9.9%), S-EXT$_{100}$ (*RCD*=~14.6%), and S-EXT$_{130}$ (*RCD*=~15.3%) with the signature reflections around $2\theta = 12.5^\circ$ and $2\theta = 20^\circ$. This implies the attendance of a V-type pattern, which is associated with the closely packed single amylose helices complexed with diverse non-polar and polar components. The extrusion 3D printing process declined the most crystalline peaks of native starch, and it showed that the ordered structures were almost totally cleaved. It was revealed that the extrusion shearing force prominently disrupts the intact crystalline structure, developing a highly amorphous structure, where the more crystalline domains only rebuild upon storage or aging [27].

There were slight changes in the characteristic peaks of LPBF 3D printed starches compared to native starch (Fig. 4d). The LPBF 3D printing mitigated the decrease of characteristic peaks, presenting a lower XRD intensity than the native starch. In this case, a fair reduction in the crystallinity degree was detected for S-LPBF$_{40}$ (*RCD*=~39%), S-LPBF$_{70}$ (*RCD*=~34%), S-LPBF$_{100}$ (*RCD*=~36%), and S-LPBF$_{130}$ (*RCD*=~32%), which fairly agree with the crystallinity degree detected by SEC (Table 1). These findings suggested that the LPBF 3D printing process possibly stabilized the crystalline packing of double-helical structures within starch. Moreover, the higher values of relative crystallinity of LPBF printed starches compared to those of extrusion 3D printed starches could be associated with the increased associations among starch chains and the rearrangement of the cleaved double helices within the crystalline regions, which cause an increase in crystal perfection or the development of new crystallite.

3.6. *In vitro starch digestion*

The reducing sugar experiment with the result of α-amylase activity was used to detect *in vitro* digestion kinetic profiles of 3D printed starch samples [38]. Fig. 5 shows starch digestibility curves obtained for different samples. The measured amount of starch digested products increased over time for extrusion of 3D printed starches and the resulting starch digestibility curves were basically first-order over the 100 min time-course. There was a reverse trend regarding LPBF 3D printed starches, where the starch digested products decreased over time. It was reported that crosslinking could slow down the *in vitro* starch digestion rate [39]. Therefore, a possible rearrangement of ordered structures in the amorphous areas of LPBF 3D printed starches may contribute to a slow *in vitro* starch digestibility. This result is in accordance with SEC NMR, and XRD measurements regarding a possible crosslinking/branching of LPBF 3D printed starches.

To measure the first-order coefficients (k), LOS fitting test was used to digestion kinetic profiles. The results revealed a single-phase *pseudo*-first-order kinetic ($R^2 > 0.90$) regarding the evaluated 3D printed samples, providing a good fit to experimental data. Table 3 shows the single rate coefficients of 3D printed starch variants along with the digestion amounts after 100 min of digestion. Evaluation of the digestion rate showed that there was a clear difference in the digestion processes between the extrusion and LPBF printed starches (Table 3). The data revealed the LPBF 3D printed samples presented a lower reducing sugar value after 100 min of digestion with a slower digestion rate. This highlights the role played by amylose in reducing hydrolysis rates in LPBF printed samples. It is highly possible that the more ordered properties induce restricting enzymic hydrolysis [38,39]. Among the LPBF printed starches, the S-LPBF$_{130}$ reveals a slower digestion rate with the lowest extent, possibly due to the presence of a more crosslinked/branched network.

3.7. *Pasting properties*

Fig. 6 depicts typical Rapid Visco-Analyzer (RVA) pasting plots for all the produced 3D printed starches. Once the starch was exposed to the heating-cooling phase in the RVA, the effects of extrusion and LPBF printing systems were simply obvious on the plots. As the temperature increased in the extrusion 3D printer, the pasting temperature (a temperature at which each granule starts to gelatinize and swell because of water absorption) was moved to the lower degrees (Fig. 6a), while this trend was reversed regarding the LPBF 3D printing process, where the pasting temperatures were shifted to the higher values (Fig. 6b). This result could be verified by the DSC experiment as it showed that the extrusion 3D printed starches had a lower gelatinization temperature, while LPBF printing led to the development of a 3D structure with a higher temperature for disorganization/melting.

The peak viscosity is another important parameter to characterize the viscosity profile of starch. It is associated with the degree of amylose leaching, swelling degree of ordered granules, amylose-lipid complex development, free water competition among leached amylose, and the

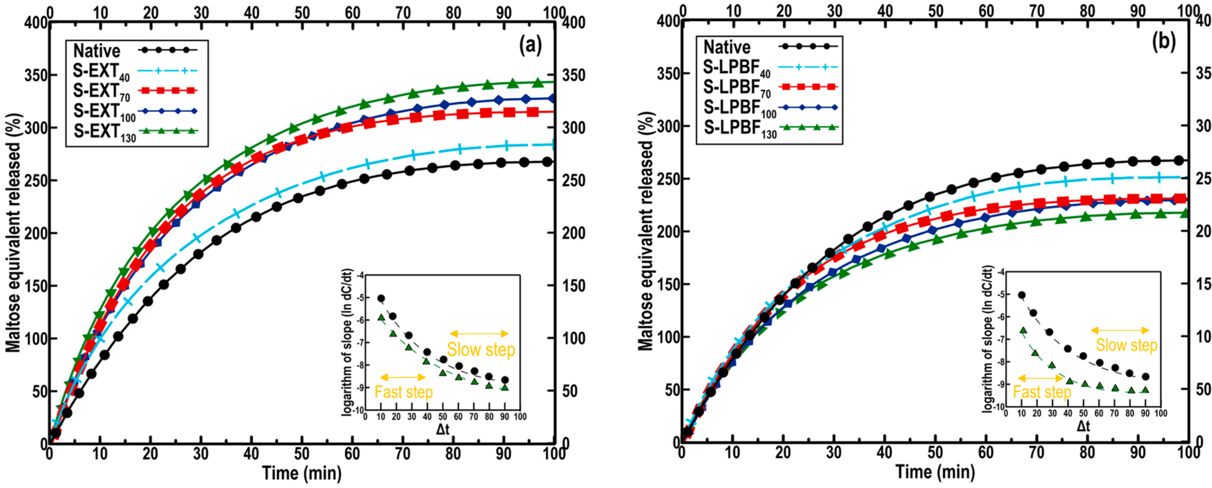

Fig. 5. Effect of extrusion (a) and LPBF (b) 3D printing systems on digestion kinetic profiles of starch. The logarithm of slope (LOS) as a function of time, in the inset for each plot, revealing that there are fast and slow phases of starch digestion.

Table 3
Kinetic parameters provided by LOS tests of *in vitro* digestibility curves and reducing sugar released extent after 100 min digestion.

Sample type	*k (min^{-1})*	*C_∞*	*R^2*	*Reducing sugar released (%)*
Native starch	0.356 ± 0.021^d	56.2 + 1.1^b	0.994 ± 0.001	0.67 ± 0.03^e
S-EXT$_{40}$	0.361 ± 0.024^e	56.2 + 1.0^b	0.997 ± 0.001	0.66 ± 0.04^e
S-EXT$_{70}$	0.376 ± 0.016 ^{f}	59.9 + 1.2^c	0.998 ± 0.002	0.71 ± 0.01 ^{f}
S-EXT$_{100}$	0.422 ± 0.014 ^{g}	63.6 + 1.3^d	0.997 ± 0.001	0.73 ± 0.04 ^{g}
S-EXT$_{130}$	0.481 ± 0.011 ^{h}	66.3 + 1.5^e	0.991 ± 0.003	0.76 ± 0.02 ^{h}
S-LPBF$_{40}$	0.322 ± 0.014^c	56.1 ± 1.5^b	0.995 ± 0.001	0.60 ± 0.04^c
S-LPBF$_{70}$	0.319 ± 0.018^c	55.7 ± 1.6^b	0.990 ± 0.001	0.63 ± 0.03^d
S-LPBF$_{100}$	0.309 ± 0.017^b	41.9 ± 1.3^a	0.997 ± 0.001	0.56 ± 0.04^b
S-LPBF$_{130}$	0.278 ± 0.016^a	42.6 ± 1.0^a	0.998 ± 0.002	0.52 ± 0.03^a

$^{a–h}$Values are the average of triplicates ± standard deviation. Different superscripts in each column show a significant statistical difference ($P < 0.05$).

residual ungelatinized granules. Based on Fig. 6a, there was no qualitative difference in the peak viscosity of S-EXT$_{40}$ and native starch. In contrast, the peak viscosity of extrusion 3D printed samples showed an increasing trend up to 70 °C (due to the occurrence of the gelatinization process) and after that, it was decreased (as a result of higher temperature and applied extrusion shearing force). As the temperature in the extrusion printer intensified on the starch, it appears that the viscosity reduced as the extrusion printing process made a partial starch degradation (*i.e.*, in S-EXT$_{100}$), and that effect was even more dramatic once the temperature changed beyond 100 °C happened (*i.e.*, S-EXT$_{130}$). It was reported that once starches were subjected to extrusion shearing force, there would be a viscosity reduction during the heating-cooling cycle with losing their crystallinity [40]. This data is also in accordance with the previously conducted SEC NMR, DSC, and XRD measurements. Compared to the extrusion 3D printing, an entirely dissimilar viscosity behavior was observed regarding the starch processed with LPBF 3D printing. In this case, the LPBF 3D printed samples showed a high viscosity along with the heating-cooling cycle, where the viscosity was increased as the surface temperature increased. This trend could be associated with increasing the stiffness of the system resulting from increasing the crystalline order, as confirmed by the frequency sweep test. Moreover, a chain interaction inside the amorphous area of starch could be developed as also revealed by NMR measurement.

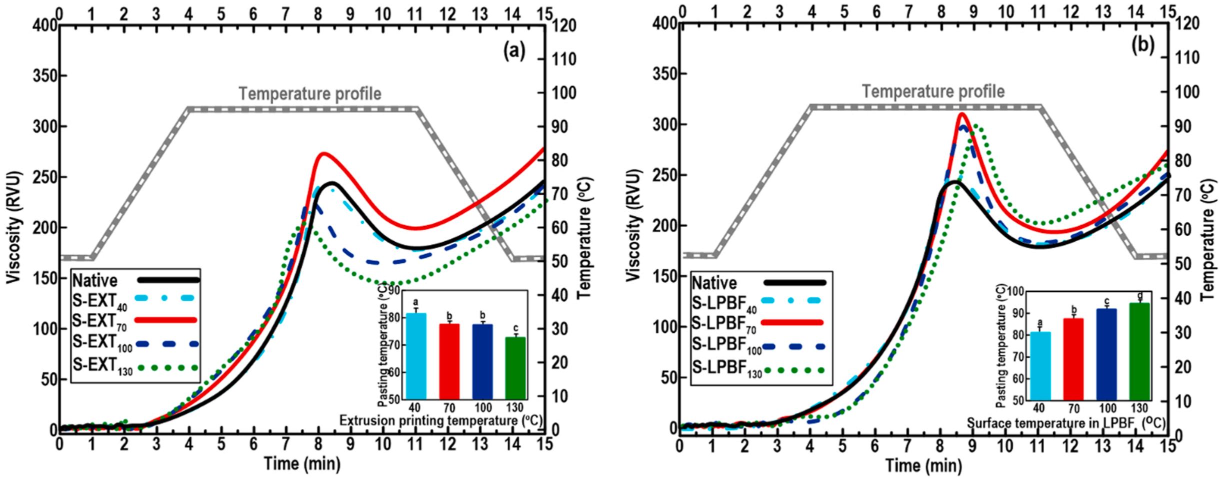

Fig. 6. Effect of printer temperature of extrusion 3D printing (a) and surface temperature of LPBF (b) on the pasting properties of starch.

3.8. *Printing performance and microstructure*

Printing performance can be assessed in the terms of the resolution of deposited layers and shape-fidelity, which is strongly associated with the flow behavior of printable inks and self-supporting features of 3D printed structures [1]. To underline the versatility of fabricated 3D printed starches, we evaluated the printing performance through the development of different 3D printed constructs. The printing quality images of each 3D printing system are shown in Fig. 7. Following 3D printing, the starch printed at 40 °C via both extrusion and LPBF 3D printers was successfully squeezed out from the nozzle or fused powders together into a 3D printed part. Then the lattice matrix (lattice square), pentagram, and gradient spacing (a rectangular waveform shape) objects were formed. However, owing to the poor viscoelastic network and the weak gel-like structure (required to support the subsequently deposited layers), whose 3D structures showed an uneven shape, which spread over the surface. It was argued that both S-EXT$_{40}$ or S-LPBF$_{40}$ were not completely gelatinized having part of the intact crystalline and lamellar structures retained. This caused the 3D printed S-EXT$_{40}$ or S-LPBF$_{40}$ to have a higher susceptibility to collapse and cracking [41]. It should be noted that we could not successfully print the native starch below 40 °C due to an inferior 3D printed structure, where it completely spread over the surface quickly.

As Fig. 7 depicted, all the LPBF 3D printed objects upheld structural integrity and shape precision compared to extrusion 3D printed starches. A conclusion for the well-defined shapes of LPBF 3D printed starches is likely ascribed to the strong gel network, stable molecular structure, and improved crystalline features of these samples. It should be mentioned that the images of printing performance concerning S-EXT$_{100}$ (or S-LPBF$_{100}$) are not shown but presented a printing quality very close to that of S-EXT$_{130}$ (or S-LPBF$_{130}$).

Compared to a single straight-line or circle structure, it is always challenging the support of set angle and geometry once quickly changing printing direction regarding the lattice square. Among all the

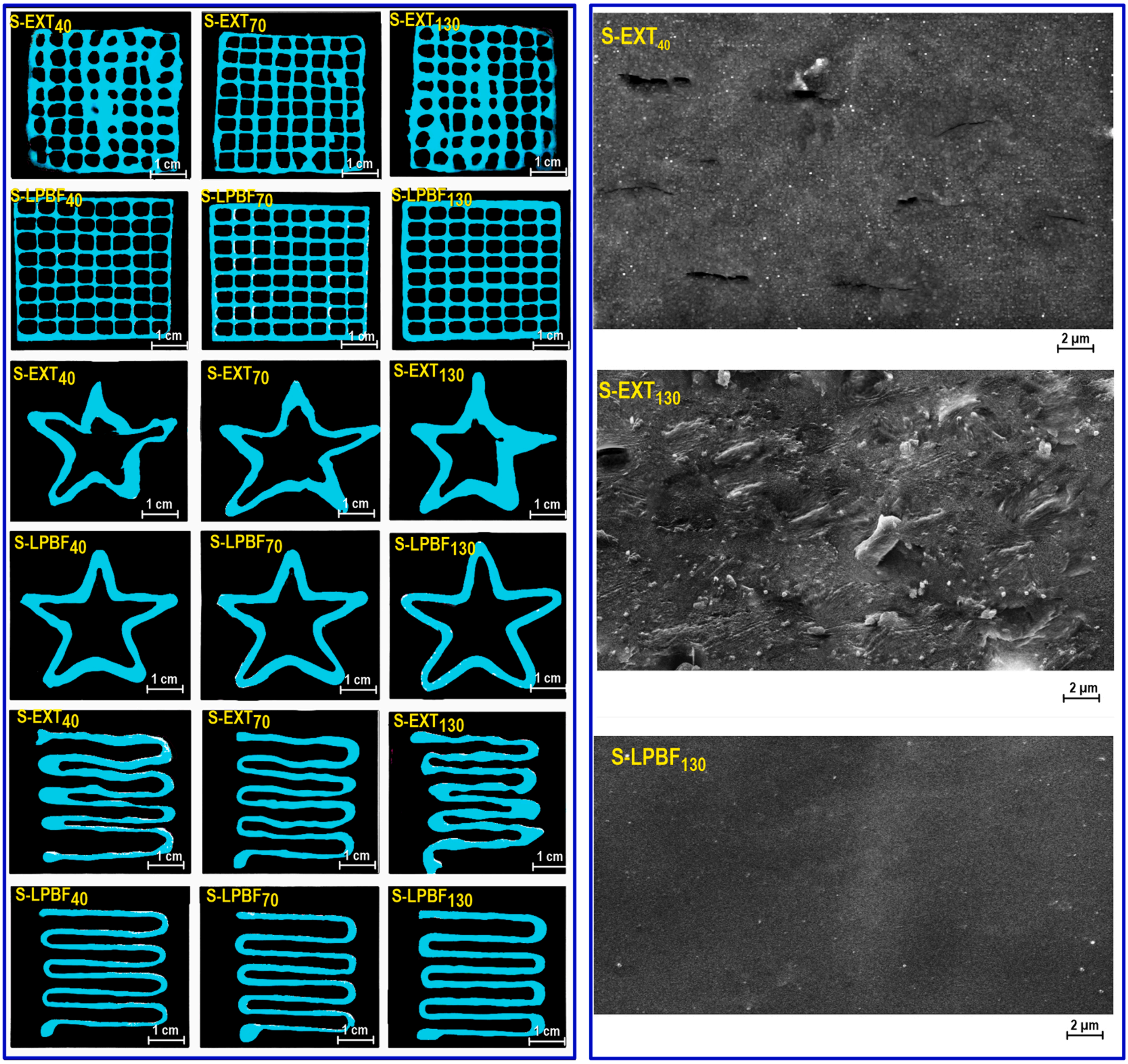

Fig. 7. Printing performance of different 3D printed starches (left) and FE-SEM micrographs (right).

evaluated 3D printed starches, the LPBF printed samples achieved superlative lattice square structures with a fair resolution (Fig. 7). The development of a complete lattice square structure with a fine geometry resulted from the self-supporting ability of LPBF printed starches in the Z-axis direction. In contrast, the 3D lattice square structures fabricated by extrusion printing showed low shape-fidelity and consequently spread around (Fig. 7). However, the S-EXT$_{70}$ presented a slightly better printing precision among the extrusion 3D printed objects. This could be due to an enhancement of collision between swollen granules and adequate chain interactions, which led to a homogeneous gel network with increased G' and low tan δ, and accordingly, high printing quality than other extrusion 3D printed starches.

With regard to the pentagram shape structures, the geometry of the meshes in S-EXT$_{40}$, S-EXT$_{100}$ (not shown), and S-EXT$_{130}$ was irregular, which is incapable to uphold the self-supporting feature in the Z-axis way. Similar to lattice square structures, the S-EXT$_{70}$ offered an improved shape than that of other extrusion printed starches. Concerning the gradient spacing structure, the straight-line were printed back and forth by changing printing direction 180° and decreasing the distance between the layers. The inferior self-supporting feature of extrusion 3D printed starches compared to LPBF 3D printing led to a lower printing precision and shape-fidelity. In this case, the printing performance results demonstrated that the gradient spacing structure regarding S-LPBF$_{100}$ (not shown) and S-LPBF$_{130}$ samples had the best printing quality, while S-EXT$_{100}$ (not shown) and S-EXT$_{130}$ showed the worst shape-fidelity (Fig. 7). In the later cases, there were not enough free starch chains in the system to undergo a chain entanglement and hydrogen bonding, leading to an uneven gel network owing to low G' and high tan δ, and thus low printing accuracy and poor strength.

By comparing the line width of 3D structures printed with extrusion and LPBF (Table S-3 in Supplementary Materials), it was detected that the line width of 3D structures increased upon the increasing temperature in the extrusion-based printer. As mentioned before, this may be caused by the poor structural strength and lower amount of connectivity, which could be verified by the frequency sweep experiment. Conversely, a decreasing line width was found for LPBF 3D printed starch (Table S-3) because of the strengthening of the matrix of 3D structure resulting from higher G'. As mentioned above, a new crystalline structure in the amorphous area of starch could be developed upon LPBF 3D printing owing to the crosslinking/branching, resulting in good mechanical stability.

Fig. 7 also shows FE-SEM photographs of selected 3D printed samples. From the FE-SEM images, the 3D printed starch processed at an extrusion printing of 40 °C (S-EXT$_{40}$) showed a non-uniform matrix with several obvious gaps and micro-cracks on its surface. A similar result was obtained for S-LPBF$_{40}$ (the image not shown). Compared to 3D printed S-EXT$_{40}$ (or S-LPBF$_{40}$), the morphological structure of S-EXT$_{130}$ seemed to be more affected by extrusion 3D printing, showing an irregular surface with some micro-cracks. This indicates that this sample suffered from degradation, in which the microstructure was damaged by the extrusion 3D printer. In contrast, the matrix of LPBF 3D printed starch (S-LPBF$_{130}$) presents an interconnected structure with a uniform structure and intact matrix (Fig. 7).

4. Conclusion

In this study, we highlighted the important role of the printing conditions on starch processability to elucidate the fact that its molecular behavior (as a highly branched polymer) changes when employed in extrusion-based or laser powder bed fusion 3D printing systems. Our data established that the type of 3D printing system employed has a critical impact on the molecular properties of starch. It was also revealed that the printer temperature of an extrusion printing system or surface temperature of a laser powder bed fusion printer plays an important role in impacting the molecular size of starch. In turn, it was found that the molecular size of starch is critical to determining certain quality parameters of the 3D printed structures, including water mobility, viscoelastic properties, thermal behavior, and crystallinity properties. We showed that a significant extent of the amylopectin fraction was degraded following the higher temperature treatment during the extrusion 3D printing process. This led to the alteration of the chain size distribution consistent with the extrusion degradation mechanism, especially when higher temperatures were involved. On the other hand, the evidence for the formation of a crosslinked structure, causing an increase in the molecular size, was observed for the starches that had undergone the laser powder bed fusion process. The more pronounced viscoelastic behavior of these samples could also be attributed to the formation of the intermolecular linkages between the starch molecules. The type of 3D printer used also showed a clear impact on starch digestibility, where the extent of starch digestion for samples processed by extrusion printing was higher compared to those involved in laser powder bed fusion. The extrusion and laser powder bed fusion processes showed an opposite thermal, crystalline, and network formation. The laser powder bed fusion produced a starch system with more crystal perfection, greater thermal stability, and better mechanical stability compared with the extrusion 3D printing process. By understanding the effects of the printer temperature in extrusion or surface temperature of laser powder bed fusion on the change (reduction or increase) of molecular weights of starch, manufacturers can design more effective 3D printing systems to formulate products with more complex desired functional properties. Future work will focus on examining the effects of other setting parameters on molecular features, so as to better understand the impacts of these process parameters on the degradation/crosslinking of polymeric material undergoing 3D printing.

Funding

Open access funding is provided by the University of Natural Resources and Life Sciences Vienna (BOKU).

CRediT authorship contribution statement

Mahdiyar Shahbazi: Writing – original draft, Validation, Resources, Methodology, Investigation, Funding acquisition, Formal analysis, Data curation, Conceptualization. **Henry Jäger:** Supervision, Investigation, Funding acquisition, Data curation, Conceptualization. **Rammile Ettelaie:** Writing – original draft, Methodology, Investigation.

Declaration of Competing Interest

The authors declare that they have no known competing financial interests or personal relationships that could have appeared to influence the work reported in this paper.

Appendix A. Supporting information

Supplementary data associated with this article can be found in the online version at doi:10.1016/j.addma.2022.102934.

References

[1] M. Shahbazi, H. Jäger, Current status in the utilization of biobased polymers for 3D printing process: a systematic review of the materials, processes, and challenges, ACS Appl. Bio Mater. 4 (2020) 325–369, https://doi.org/10.1021/acsabm.0c01379.

[2] M. Shahbazi, H. Jäger, R. Ettelaie, Application of Pickering emulsions in 3D printing of personalized nutrition. Part I: development of reduced-fat printable casein-based ink, Colloids Surf. A Physicochem. Eng. 622 (2021), 126641, https://doi.org/10.1016/j.colsurfa.2021.126641.

[3] M. Shahbazi, H. Jäger, S.J. Ahmadi, M. Lacroix, Electron beam crosslinking of alginate/nanoclay ink to improve functional properties of 3D printed hydrogel for removing heavy metal ions, Carbohydr. Polym.. 240 (2020), 116211, https://doi.org/10.1016/j.carbpol.2020.116211.

[4] F.C. Godoi, S. Prakash, B.R. Bhandari, 3D printing technologies applied for food design: status and prospects, J. Food Eng. 179 (2016) 44–54, https://doi.org/10.1016/j.jfoodeng.2016.01.025.

[5] N. Shahrubudin, T.C. Lee, R. Ramlan, An overview on 3D printing technology: technological, materials, and applications, Procedia Manuf. 35 (2019) 1286–1296, https://doi.org/10.1016/j.promfg.2019.06.089.

[6] T. Wohlers, Wohlers report 2016, Wohlers Associates, Inc.,, 2016.

[7] A. Awad, F. Fina, A. Goyanes, S. Gaisford, A.W. Basit, 3D printing: principles and pharmaceutical applications of laser powder bed fusion, Int. J. Pharm. 586 (2020), 119594, https://doi.org/10.1016/j.ijpharm.2020.119594.

[8] A. Ahlinder, T. Fuoco, Á. Morales-López, M.A. Yassin, K. Mustafa, A. Finne-Wistrand, Nondegradative additive manufacturing of medical grade copolyesters of high molecular weight and with varied elastic response, J. Appl. Polym. Sci. 137 (2020) 48550, https://doi.org/10.1002/app.48550.

[9] B. Scherer, I.L. Kottenstedde, W. Bremser, F.M. Matysik, Analytical characterization of polyamide 11 used in the context of laser powder bed fusion: physico-chemical correlations, Polym. Test. 91 (2020), 106786, https://doi.org/10.1016/j.polymertesting.2020.106786.

[10] K. Wudy, D. Drummer, Aging effects of polyamide 12 in laser powder bed fusion: molecular weight distribution and thermal properties, Addit. Manuf. 25 (2019) 1–9, https://doi.org/10.1016/j.addma.2018.11.007.

[11] S. Sun, X. Gan, Z. Wang, D. Fu, W. Pu, H. Xia, Dynamic healable polyurethane for laser powder bed fusion, Addit. Manuf. 33 (2020), 101176, https://doi.org/10.1016/j.addma.2020.101176.

[12] R.A. Cave, S.A. Seabrook, M.J. Gidley, R.G. Gilbert, Characterization of starch by size-exclusion chromatography: the limitations imposed by shear scission, Biomacromolecules 10 (2009) 2245–2253, https://doi.org/10.1021/bm900426n.

[13] N.V. Minaev, T.S. Demina, S.A. Minaeva, A.A. Dulyasova, E.D. Minaeva, S. A. Gonchukov, T.A. Akopova, P.S. Timashev, The Evolution of Surface-Laser powder bed fusion: modifying and Forming 3D Structures for Tissue Engineering, Bull. Russ. Acad. Sci.: Phys. 11 (2020) 1315–1320, https://doi.org/10.3103/S1062873820110192.

[14] G. Craft, J. Nussbaum, N. Crane, J.P. Harmon, Impact of extended sintering times on mechanical properties in PA-12 parts produced by powderbed fusion processes, Addit. Manuf. 22 (2018) 800–806, https://doi.org/10.1016/j.addma.2018.06.028.

[15] S. Ziegelmeier, F. Wöllecke, C.J. Tuck, R.D. Goodridge, R.J. Hague, Aging behavior of thermoplastic elastomers in the laser sintering process, J. Mater. Res. 29 (2014) 1841–1851, https://doi.org/10.1557/jmr.2014.172.

[16] L. Verbelen, S. Dadbakhsh, M. Van den Eynde, D. Strobbe, J.P. Kruth, B. Goderis, P. Van Puyvelde, Analysis of the material properties involved in laser sintering of thermoplastic polyurethane, Addit. Manuf. 15 (2017) 12–19, https://doi.org/10.1016/j.addma.2017.03.001.

[17] J. Singh, A. Dartois, L. Kaur, Starch digestibility in food matrix: a review, Trends Food Sci. Technol. 21 (2010) 168–180, https://doi.org/10.1016/j.tifs.2009.12.001.

[18] N. Singh, J. Singh, L. Kaur, N.S. Sodhi, B.S. Gill, Morphological, thermal and rheological properties of starches from different botanical sources, Food Chem. 81 (2003) 219–231, https://doi.org/10.1016/S0308-8146(02)00416-8.

[19] AACC. Approved Methods, tenth ed., The American Association of Cereal Chemists, St. Paul, MN, 2000.

[20] W.R. Morrison, B. Laignelet, An improved colorimetric procedure for determining apparent and total amylose in cereal and other starches, J. Cereal Sci. 1 (1983) 9–20, https://doi.org/10.1016/S0733-5210(83)80004-6.

[21] M. Shahbazi, H. Jäger, R. Ettelaie, Development of an antioxidative pickering emulsion gel through polyphenol-inspired free-radical grafting of microcrystalline cellulose for 3D food printing, Biomacromolecules 22 (2021) 4592–4605, https://doi.org/10.1021/acs.biomac.1c00896.

[22] F. Fina, A. Goyanes, S. Gaisford, A.W. Basit, Laser powder bed fusion (LPBF) 3D printing of medicines, Int. J. Pharm. 529 (2017) 285–293, https://doi.org/10.3390/pharmaceutics12020110.

[23] J. Hasjim, G.C. Lavau, M.J. Gidley, R.G. Gilbert, In vivo and in vitro starch digestion: are current in vitro techniques adequate? Biomacromolecules 11 (2010) 3600–3608, https://doi.org/10.1021/bm101053y.

[24] F. Vilaplana, R.G. Gilbert, Characterization of branched polysaccharides using multiple-detection size separation techniques, J. Sep. Sci. 33 (2010) 3537–3554, https://doi.org/10.1002/jssc.201000525.

[25] M. Kiumarsi, M. Shahbazi, S. Yeganehzad, D. Majchrzak, O. Lieleg, B. Winkeljann, Relation between structural, mechanical and sensory properties of gluten-free bread as affected by modified dietary fibers, Food Chem. 277 (2019) 664–673, https://doi.org/10.1016/j.foodchem.2018.11.015.

[26] M. Kiumarsi, D. Majchrzak, H. Jäger, J. Song, O. Lieleg, M. Shahbazi, Comparative study of instrumental properties and sensory profiling of low-calorie chocolate containing hydrophobically modified inulin. Part II: proton mobility, topological, tribological and dynamic sensory properties, Food Hydrocoll. 110 (2021), 106144, https://doi.org/10.1016/j.foodhyd.2020.106144.

[27] M. Shahbazi, M. Majzoobi, A. Farahnaky, Impact of shear force on functional properties of native starch and resulting gel and film, J. Food Eng. 223 (2018) 10–21, https://doi.org/10.1016/j.jfoodeng.2017.11.033.

[28] M. Shahbazi, H. Jäger, R. Ettelaie, Application of Pickering emulsions in 3D printing of personalized nutrition. Part II: functional properties of reduced-fat 3D printed cheese analogues, Colloids Surf. A Physicochem. Eng. 624 (2021), 126760, https://doi.org/10.1016/j.colsurfa.2021.126760.

[29] P.J. Butterworth, F.J. Warren, T. Grassby, H. Patel, P.R. Ellis, Analysis of starch amylolysis using plots for first-order kinetics, Carbohydr. Polym. 87 (2012) 2189–2197, https://doi.org/10.1016/j.carbpol.2011.10.048.

[30] R. Moretti, J.S. Thorson, A comparison of sugar indicators enables a universal high-throughput sugar-1-phosphate nucleotidyltransferase assay, Anal. Biochem. 377 (2008) 251–258, https://doi.org/10.1016/j.ab.2008.03.018.

[31] Y. Liu, J. Chen, S. Luo, C. Li, J. Ye, C. Liu, R.G. Gilbert, Physicochemical and structural properties of pregelatinized starch prepared by improved extrusion cooking technology, Carbohydr. Polym. 175 (2017) 265–272, https://doi.org/10.1016/j.carbpol.2017.07.084.

[32] M. Shahbazi, H. Jäger, R. Ettelaie, A promising therapeutic soy-based pickering emulsion gel stabilized by a multifunctional microcrystalline cellulose: application in 3D food printing, J. Agric. Food Chem. 70 (2022) 2374–2388, https://doi.org/10.1021/acs.jafc.1c05644.

[33] V.J. Davidson, D. Paton, L.L. Diosady, G. Larocque, Degradation of wheat starch in a single screw extruder: characteristics of extruded starch polymers, J. Food Sci. 49 (1984) 453–458, https://doi.org/10.1111/j.1365-2621.1984.tb12441.x.

[34] T.T. Tran, K.J. Shelat, D. Tang, E. Li, R.G. Gilbert, J. Hasjim, Milling of rice grains. The degradation on three structural levels of starch in rice flour can be independently controlled during grinding, J. Agric. Food Chem. 59 (2011) 3964–3973, https://doi.org/10.1021/jf105021r.

[35] M. Li, J. Hasjim, F. Xie, P.J. Halley, R.G. Gilbert, Shear degradation of molecular, crystalline, and granular structures of starch during extrusion, Starch-Stärke 6 (2014) 595–605, https://doi.org/10.1002/star.201300201.

[36] M. Shahbazi, H. Jäger, R. Ettelaie, J. Chen, Construction of 3D printed reduced-fat meat analogue by biosurfactants. Part I: flow behavior, thixotropic feature, and network structure of soy protein-based inks, Food Hydrocoll. 120 (2021), 106967, https://doi.org/10.1016/j.foodhyd.2021.106967.

[37] M.H. Tunick, Small-strain dynamic rheology of food protein networks, J. Agric. Food Chem. 59 (2011) 1481–1486, https://doi.org/10.1021/jf1016237.

[38] F.J. Warren, B. Zhang, G. Waltzer, M.J. Gidley, S. Dhital, The interplay of α-amylase and amyloglucosidase activities on the digestion of starch in in vitro enzymic systems, Carbohydr. Polym. 117 (2015) 192–200, https://doi.org/10.1016/j.carbpol.2014.09.043.

[39] L. Ding, Q. Huang, W. Xiang, X. Fu, B. Zhang, J.Y. Wu, Chemical cross-linking reduces in vitro starch digestibility of cooked potato parenchyma cells, Food Hydrocoll. 124 (2022), 107297, https://doi.org/10.1016/j.foodhyd.2021.107297.

[40] J. Guan, M.A. Hanna, Extruding foams from corn starch acetate and native corn starch, Biomacromolecules 5 (2004) 2329–2339, https://doi.org/10.1021/bm049512m.

[41] M. Shahbazi, H. Jäger, R. Ettelaie, Development of an antioxidative pickering emulsion gel through polyphenol-inspired free-radical grafting of microcrystalline cellulose for 3D food printing, Biomacromolecules 22 (2021) 4592–4605, https://doi.org/10.1021/acs.biomac.1c00896.